ISPRS Journal of Photogrammetry and Remote Sensing 129 (2017) 200–211

Contents lists available at ScienceDirect

ISPRS Journal of Photogrammetry and Remote Sensing

journal homepage: www.elsevier.com/locate/isprsjprs

A linearly approximated iterative Gaussian decomposition method for waveform LiDAR processing

Giorgos Mountrakis *, Yuguang Li

Department of Environmental Resources Engineering, State University of New York, College of Environmental Science and Forestry, 1 Forestry Drive, Syracuse, NY 13210, United States

ARTICLE INFO

Article history:
Received 19 January 2017
Received in revised form 9 May 2017
Accepted 9 May 2017
Available online 18 May 2017

Keywords:
Full-waveform
Gaussian decomposition
LVIS sensor
Stepwise iteration
Piecewise linear approximation

ABSTRACT

Full-waveform LiDAR (FWL) decomposition results often act as the basis for key LiDAR-derived products, for example canopy height, biomass and carbon pool estimation, leaf area index calculation and under canopy detection. To date, the prevailing method for FWL product creation is the Gaussian Decomposition (GD) based on a non-linear Levenberg-Marquardt (LM) optimization for Gaussian node parameter estimation. GD follows a "greedy" approach that may leave weak nodes undetected, merge multiple nodes into one or separate a noisy single node into multiple ones. In this manuscript, we propose an alternative decomposition method called Linearly Approximated Iterative Gaussian Decomposition (LAIGD method). The novelty of the LAIGD method is that it follows a multi-step "slow-and-steady" iterative structure, where new Gaussian nodes are quickly discovered and adjusted using a linear fitting technique before they are forwarded for a non-linear optimization. Two experiments were conducted, one using real full-waveform data from NASA's land, vegetation, and ice sensor (LVIS) and another using synthetic data containing different number of nodes and degrees of overlap to assess performance in variable signal complexity. LVIS data revealed considerable improvements in RMSE (44.8% lower), RSE (56.3% lower) and rRMSE (74.3% lower) values compared to the benchmark GD method. These results were further confirmed with the synthetic data. Furthermore, the proposed multi-step method reduces execution times in half, an important consideration as there are plans for global coverage with the upcoming Global Ecosystem Dynamics Investigation LiDAR sensor on the International Space Station.

1. Introduction

Airborne laser scanning (ALS), also referred to as LiDAR or laser radar, offers promising capabilities in a wide variety of environmental applications (Mallet and Bretar, 2009). Compared with traditional photogrammetry surveying techniques, laser scanner observes through the land cover and achieves the vertical profiles of its target in-depth. By means of radiative transfer theory, the shapes of echoes could potentially be translated into the geometric distribution and physical properties of different object layers or surfaces along the track (Wagner et al., 2006). While several studies have offered global land cover products (Grekousis et al., 2015) and land cover classification methods have been evaluated (Khatami et al., 2016) LiDAR data offer additional land cover monitoring capabilities.

The detection ability of a LiDAR system is dependent on a range of factors. A fully recorded backscattered waveform allows more control and flexibility in processing the interaction history of transmitted pulses. Thereby, full-waveform LiDAR, which provides full records of echoes, provides increased opportunity to discover and understand the structural diversity of land cover surfaces. Researchers have successfully used mathematical tools to interpret study areas as different land cover surfaces by separating echoes from LiDAR full-waveform. Structural properties of different land surfaces could be understood from the shape and position of each echo (Wagner et al., 2006). One example sensor is the airborne Land, Vegetation, and Ice Sensor (LVIS). LVIS is typically flown at an altitude that results in footprint diameter of 10–25 m, and the space-borne ICESat (Ice, Cloud, and land Elevation Satellite) captures footprints of 70 m in diameter (Drake et al., 2002). Full-waveform LiDAR is particularly interesting because of its' ability to penetrate canopy and reach the ground. This advantage is significant in observing regions with dense vegetation, where only few

* Corresponding author.
E-mail address: gmountrakis@esf.edu (G. Mountrakis).

http://dx.doi.org/10.1016/j.isprsjprs.2017.05.009

out of several thousand returns may be reflected from the ground (Blair and Hofton, 1999a).

These penetrating characteristics have lead remote sensing of full-waveform LiDAR detection to a broad range of applications. The dominant domain has been forestry applications, for a review see Wulder et al. (2012). Depending on the applied spatial scale, applications include segmenting individual tree crowns (Persson et al., 2002; Reitberger et al., 2008a; Liu et al., 2015; Strîmbu and Strîmbu, 2015), classifying vegetation species (Ranson et al., 2004; Reitberger et al., 2008b) and separating vegetation from non-vegetation classes (Ducic et al., 2006). Another common application resides in biomass estimation using exclusively LiDAR data (Ahmed et al., 2013; Montesano et al., 2013; Zhuang et al., 2015) or fusion with other sensors (Swatantran et al., 2011; Sun et al., 2011; Montesano et al., 2014), as well as biomass dynamics over time (Hudak et al., 2012; Huang et al., 2013). Extensive efforts have been placed in vertical structure identification, including top height and ground peak identification (Sun and Ranson, 2000; Yu et al., 2004; Harding et al., 2001; Lefsky et al., 1999; Lim et al., 2003; Castillo-Núñez et al., 2011; Wang et al., 2014; Zhuang and Mountrakis, 2014a, 2014b; Sullivan et al., 2014; Castillo et al., 2012; Hancock et al., 2011; Hayashi et al., 2013; Chen, 2010). Other application domains include urban areas (Jutzi and Stilla, 2003; Jutzi and Stilla, 2005a, 2005b; Gong et al., 2011; Mallet et al., 2011; Slota, 2015; Alexander et al., 2010), ice studies (Schenk et al., 2014; Yi et al., 2015), leaf area index estimation (Tang et al., 2012, 2014, 2016), bathymetric studies (Wang et al., 2015), power line surveys (Matikainen et al., 2016). Studies also investigated specific applications of small-footprint full waveform data (Wagner, 2010; Höfle et al., 2012; Fieber et al., 2015) along with fusion with hyperspectral data (Wang and Glennie, 2015; Suomalainen et al., 2011) and compression of the high volume full waveform data (Jóźków et al., 2014).

From interpolation perspective, the returned waveforms are typically modeled by mathematical equations. In most cases, echoes are approximated as separate Gaussian functions, which could be interpreted as the convoluted product between a system waveform (assumed to be of Gaussian shape with a calibrated width) and a surface scattering function (Wagner et al., 2006). The backscattered full-waveforms, which could also be interpreted as echoes of active LiDAR light source from different objects, are then decomposed into the sum of several separate Gaussian nodes. Persson et al. (2005) proposed a waveform processing method based on the Expectation-Maximization algorithm (EM) (Dempster et al., 1977). This algorithm optimizes the parameters of each Gaussian node by using a two-stage iteration, namely E step & M step. The expectation of the likelihood is computed in E step and then used in M step to get maximized. After the initial values (including the number of Gaussian components and shape parameters) are predicted and inserted into the algorithm, the process would be repeated until the likelihood expectation stops increasing. Hofton et al. (2000) proposed to apply Levenberg-Marquardt (LM) optimization in precisely estimating the parameters of Gaussian nodes. The initial estimates of Gaussian function parameters are predicted by zero-crossing features of first and second derivatives. During the prediction process, a filtering step and a selection step are carried out to increase the accuracy of initial values and to ensure the significance of each Gaussian node. However, like any non-linear optimization process, selection of initial parameters and local maxima trapping often restrict LM optimization from achieving the best fit. Furthermore, coarse peak detection as they discussed is sometimes incapable of detecting weak nodes hidden in other overlapping nodes. To solve this problem, Chauve et al. (2007) proposed an iterative approach, in which new Gaussian nodes are detected and added from the difference between the raw and simulated waveforms. However, the bias from optimized parameters could sometimes bring too many peaks in the produced residual waveform, which may lead to redundant nodes, inaccurate fitting and low computational efficiency. Wang et al. (2013) achieved signal decomposition using wavelets and it was tested on GLAS data. Other Gaussian-based decomposition methods have been proposed (Harding and Carabajal, 2005; Duong et al., 2008) along with more generalized functions (Mallet and Bretar, 2009) or localization techniques (Roncat et al., 2011). Jutzi and Stilla (2006) and Wang et al. (2009) investigated convolution in the time domain as a means of signal decomposition.

In this paper, we propose an iterative method, named linearly approximated iterative Gaussian decomposition (LAIGD), to improve Gaussian decomposition of backscattered full-waveforms in terms of accuracy and execution time. Our hypothesis is that an additional iterative linear fitting step before a non-linear LM optimization steps would improve LiDAR signal decomposition over the existing prevailing method using non-linear LM optimization only.

2. Methods

2.1. Approach overview

A challenge of signal un-mixing models is to discover as many weak Gaussian nodes while reducing identification of non-existent redundant nodes. Hofton et al. (2000) proposed a Levenberg-Marquardt (LM) based optimization for parameter estimation on detected Gaussian nodes. Initial Gaussian node parameters are optimized by a final non-negative gradient descent adjustment, the LM optimization. However, LM optimizer might be stuck in a locally optimized state due to insufficient or biased initial parameters. A Gaussian mixture, in this case, might be fitted as the summation of several Gaussian nodes of incorrect standard deviations and centroids. The estimated Gaussian mixture sometimes includes a higher number than the correct Gaussian node count due to over-fitting, which considerably reduces the accuracy performance. However, with closer initial estimated Gaussian node parameters, the un-controlled LM optimization might not only adjust the Gaussian parameters towards higher accuracy, but may be able to detect Gaussian nodes which initially were not discovered. In this paper, we propose a novel method to generate initial parameters before the LM optimization process takes place. The proposed method increases the chance to discover hidden nodes while reducing the chance of generating repeated nodes. In doing so, the initial parameter values are closer to the optimal values thus improving fitting accuracy and reduced execution time.

2.2. Processing details

We decompose the backscattered waveform signal (a time-series 1D point sequence $y(t)$) into the sum of several different Gaussian functions characterized by amplitude a_i, centroid c_i and standard deviation δ_i. The fitted Gaussian mixture model could be represented in the form

$$y = f(x) = \sum_{i=1}^{n} a_i e^{-(x-c_i)^2/2\delta_i^2} \quad (1)$$

The proposed LAIGD method iteratively calculates and adjusts the number of Gaussian functions n and their parameters $\{a_i, c_i, \delta_i\}$ in the fitting function, such that the root-mean-square error (RMSE) between the raw time-series waveform and the sum of Gaussian functions is minimized. The RMSE measurement is expressed as

$$\varepsilon = \sqrt{\frac{1}{T}\sum_{k=1}^{T}(f(t_k) - y_k)^2} \quad (2)$$

where T indicates the number of sampling points t_k from the fitted waveform.

The following criteria are followed to restrict and evaluate the fitting process (Hofton et al., 2000):

a. The standard deviation of simulated Gaussian nodes should be no less than the standard deviation of the transmitted Gaussian pulse.
b. The fitted waveform is accepted only when the standard deviation of the fitting error is less than three times the standard deviation of the background noise signal within the observed waveform.

Our proposed pipeline are presented in the flowchart of Fig. 1. Three major steps take place in the following order: Waveform Pre-processing S_{pre}, Iterative Linear Fitting S_{lin} and Non-linear Fitting S_{nlin}. In Waveform Pre-processing S_{pre}, the noisy input waveform is analyzed so that active low-frequency echoes are smoothened and steady background noise is reduced in high frequency. From the Iterative Linear Fitting step S_{lin}, a wide range of Gaussian nodes are tested and a good approximation of the final Gaussian parameters are chosen. In Non-linear Fitting S_{nlin}, the Gaussian nodes selected from S_{lin} are fed into a final non-linear optimizer. A conditional final node fitting step is followed as the final step to potentially discover new nodes from residuals.

2.2.1. Waveform pre-processing step S_{pre}

The returned waveform signals are often mixed with white Gaussian background noise of relatively steady standard deviation, where only a small proportion is considered as the actively returned waveform. During this pre-processing step, waveforms are segmented with a threshold criterion, where the active echo signals and steady background noise signals are separated. The active echo signals are those points with responses three times greater than the standard deviation of the background noise. The steady background noise signals are considered as the beginning and ending segments of the waveform signals, which are between the transmitted pulse and active echo signal. The active echo signals are then smoothed by a triangle filter of a standard deviation of twice as much as the standard deviation of the transmitted LiDAR pulse.

2.2.2. Iterative linear fitting step S_{lin}

Initially in our waveform fitting, we assumed that each Gaussian node is superimposed on a complete or a piecewise first-order linear function (a straight line segment). We detect nodes and generate their initial parameters in the step of Initial Gaussian Node Parameterization S_{lin_1}. These detected Gaussian nodes are then assumed to be superimposed on the response from its adjacent Gaussian nodes with certain curvatures. Based on the amount of deformation each detected node received from its neighbors, we adjust these node subsequently with a linear algorithm in an optimized order. We call these steps the Linear Fitting Procedure S_{lin_2}. Residuals are then computed between the simulated waveform and the pre-processed waveform, and fed back to the Linear Fitting Procedure S_{lin_2} until no Gaussian node could be detected. The whole iterative step is called the Iterative Linear Fitting Step S_{lin}. These adjusted nodes would eventually be used in the non-linear fine optimization stage S_{nlin}.

2.2.2.1. Initial Gaussian node parameterization S_{lin_1}. Depending on the amplitude of Gaussian nodes along with their relative positions, each Gaussian center node would either show up as a local/global maximum or be obscured by the high responses from its adjacent nodes. During the node search process (i.e. center location identification), our method only considers the local maxima along with their nearby ranges as a waveform segment to parameterize each node. The range of each node (i.e. length in time) is computed from the derivatives of smoothed waveform generated by pre-processing step S_{pre}. At first, closest inflection point pair (zero crossing point of second derivative) is detected around local maximum (black dots in Fig. 2). The beginning and ending points of the range are set for cropping when the absolute slope value of each goes below one fifth of their corresponding inflection point. The one fifth value was empirically assigned to include the majority of the Gaussian node while preventing inclusion of adjacent Gaussian nodes. In Fig. 2 the range of the left node is the portion of the waveform between the two red triangles. For each node, its corresponding range is identified as above and only the waveform in this range is used for further parameterization for that node. In the example of Fig. 2, only the waveform between the two red triangles will be cropped and used for parameterization of the node centered at 50 ns.

Our working assumption is that the node parameters $\{a_i, c_i, \delta_i\}$ could be estimated by looking at the positions and intensity of the inflection point pairs $(x_{inflpt.left}, y_{inflpt.left})$ and $(x_{inflpt.right}, y_{inflpt.right})$ and adding a constant offset to simulate potential mixed Gaussians. The constant number 0.393 in equation (5) is the ratio from the Gaussian response difference between centroid and one standard deviation position to the Gaussian response of centroid ($i.e. 1 - \exp(-0.5)$). Variable y_{c_i} is the response of node i at center c.

$$\delta_i = |x_{inflpt.right} - x_{inflpt.left}|/2 \quad (3)$$

$$c_i = (x_{inflpt.left} + x_{inflpt.right})/2 \quad (4)$$

$$a_i = (y_{c_i} - (y_{inflpt.left} + y_{inflpt.right})/2)/0.393 \quad (5)$$

In cases where significant mixing between nodes exists, the identification of symmetrical inflection points from both sides may not be available. To compensate, we assume the Gaussian bell shape is preserved only on a single side and only that side should be used in initial parameter estimation. The amplitude a_i, standard deviation δ_i and centroid position c_i are then given by

$$a_i = (y_{Lc.Max} - y_{Inflection\ pt.})/0.393 \quad (6)$$

$$\delta_i = |x_{Lc.Max} - x_{Inflection\ pt.}| \quad (7)$$

$$c_i = x_{Lc.Max} \quad (8)$$

where $x_{Lc.Max}$ and $y_{Lc.Max}$ are position and intensity values of the local maxima point. $x_{Inflection\ pt.}$ and $y_{Inflection\ pt.}$ are the position and intensity of the inflection point on their corresponding side. To decide if we should perform initial Gaussian node parameterization S_{lin_1} only using a single side or both sides from a peak point, we take advantage of the symmetrical property of a Gaussian distribution by examining two sets of variables:

i. Horizontal distance between local maxima point and the closest inflection points on two sides of the local maxima.

$$\Delta x_{left} = |x_{Lc.Max} - x_{Inflection\ pt.left}| \quad (9)$$

$$\Delta x_{right} = |x_{Lc.Max} - x_{Inflection\ pt.right}| \quad (10)$$

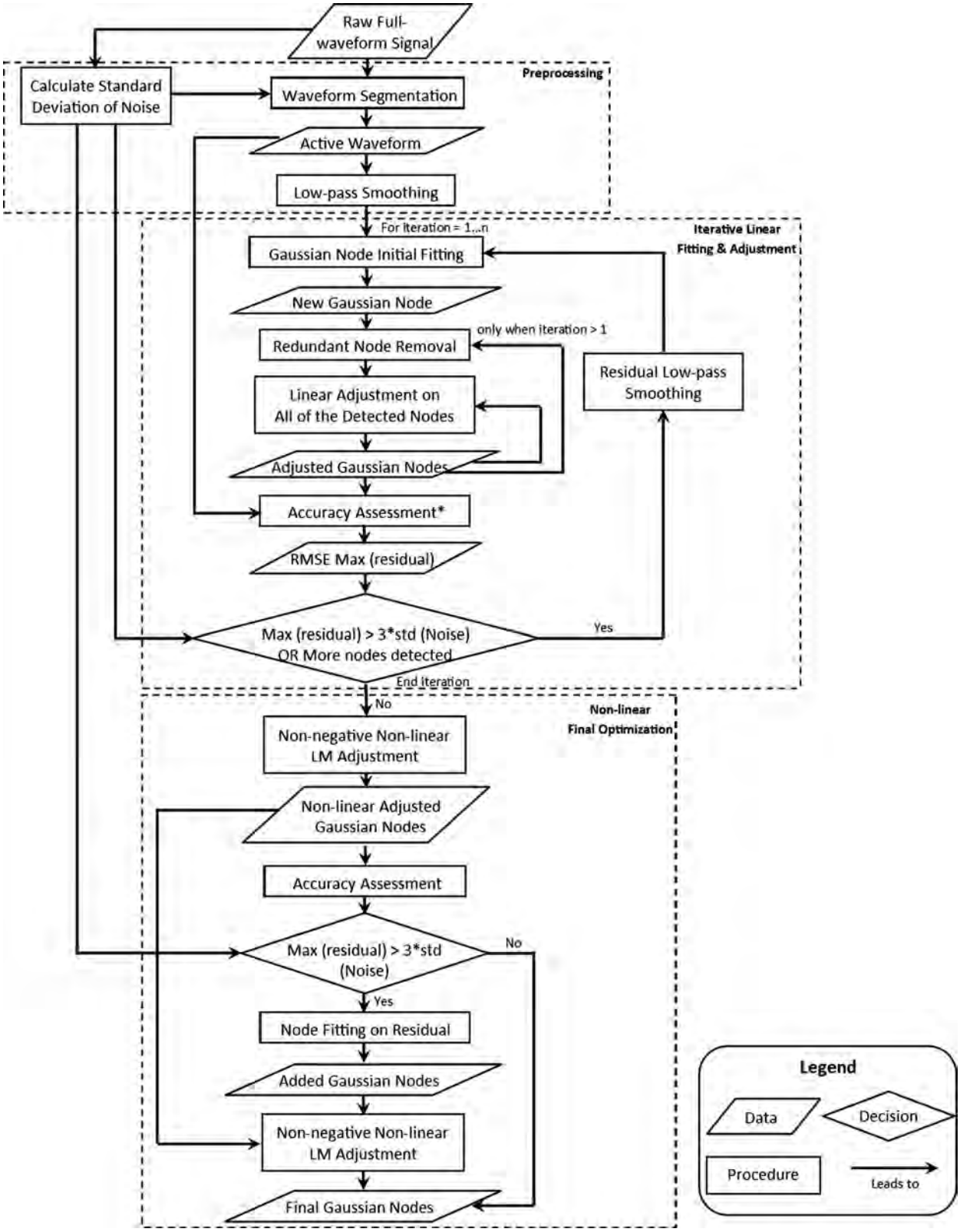

Fig. 1. Flowchart of the LAIGD method.

ii. Mean intensity on two segments $[x_{Lc.Max} - \min(\Delta x_{left}, \Delta x_{right}), x_{Lc.Max}]$ and $[x_{Lc.Max}, x_{Lc.Max} + \min(\Delta x_{left}, \Delta x_{right})]$. They are denoted as

$$\overline{y_{left}} = \overline{y_{[x_{Lc.Max} - \min(\Delta x_{left}, \Delta x_{right}), x_{Lc.Max}]}} \quad (11)$$

$$\overline{y_{right}} = \overline{y_{[x_{Lc.Max}, x_{Lc.Max} + \min(\Delta x_{left}, \Delta x_{right})]}} \quad (12)$$

When either Δx_{left} or Δx_{right} is smaller than the empirical value of two thirds of the other, we assume that the node of this waveform segment is asymmetrical. The side of the lower values between $\overline{y_{left}}$

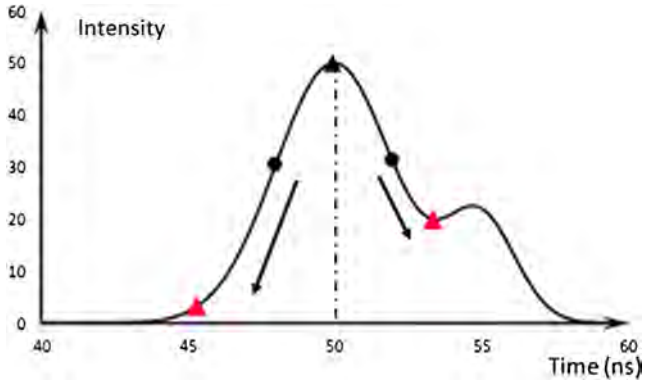

Fig. 2. Local segmentation of the Gaussian component.

and $\overline{y_{right}}$ would be used along with Eqs. (6)–(8) in the initial parameterization. On the other hand, when Δx_{left} and Δx_{right} are close enough (exclusive from the condition above), Eqs. (3)–(5) would be used on the cropped waveform, thus including both sides.

2.2.2.2. Redundant node reduction. Node removal takes place to address two issues: (1) a node with very weak responses, (2) a node with nearby very similar nodes. In the first case, a Gaussian node is removed if its area is smaller than three percent of the area under the complete input waveform. The threshold value of 3% is balancing noise removal with actual response preservation. To avoid the latter case new node candidates are compared with all previously detected nodes. The pairs with both standard deviation ratios between [0.5, 2], and relative centroid distance under 1.5 are recognized as node pairs of high similarity. These two thresholds are empirically set to reduce the likelihood of over-interpreting the observed waveform by minimizing the number of Gaussians needed for the decomposition. Similar criteria have been mentioned in Chauve et al. (2007). The node candidate included in this pair is therefore not added. Relative centroid distance Δ_{cent} is defined as:

$$\Delta_{cent} = \frac{|c_i - c_j|}{max(\delta_i, \delta_j)} \tag{13}$$

2.2.2.3. Linear adjustment of detected nodes S_{lin_2}. The estimated parameters from $\boldsymbol{S_{lin\_1}}$ are generated based on the assumption that each Gaussian node during the fitting process is superimposed on a first-order linear function (straight-line segment). However, the bell shape of a Gaussian node is sometimes strongly deformed by the response of other Gaussian nodes, especially from the range of high curvature. Initial parameter estimates from these deformed Gaussian shapes might mislead the optimizer into a state of local maxima error, which generates inaccurate Gaussian node estimates. Even though iterative non-linear optimization is designed to optimize biased initial parameters and discover the hidden nodes from parameter optimization, shape deformation sometimes cause excessive initial parameters and lead non-linear optimization to an over-fitted solution, which includes incorrect Gaussian Node estimates and significantly higher execution time.

To address this, a quick adjustment is incorporated in the fitted Gaussian nodes by simulating the superimposed response from adjacent Gaussian nodes. The simulated response substitutes the linear function with a curve. The retained Gaussian features help fine-tune the initial estimation of each Gaussian node.

Specifically, the method subtracts the fitted single Gaussian waveforms from the complete input signal. At this stage, the residual contains bias of adjacent nodes, waveform of the component which is currently being adjusted and sometimes undiscovered nodes. The method segments the un-deformed portion of the component currently being adjusted, which is a bell-shaped peak close to its current center. Parameters $\{a_i, c_i, \delta_i\}$ are then re-estimated by using a non-negative least-square Gaussian fitting technique, or, if the condition for the previous choice is not satisfied, by using the derivative features method involving the inflection points discussed earlier.

The choice of which fitting method as we mentioned above is made by considering the following cases. When a single Gaussian node in the local segment is only added on a weak response, the method assumes that this local segment contains a Gaussian node along with random noise. Non-negative least-square Gaussian fitting is applied on the segment to solve for the standard deviation, where amplitude and centroid could be identified directly from the shape. Specifically, when the response of any local range point is below the response of the local maxima point $y_{Lc.Max}$, but above one fifth of $y_{Lc.Max}$, the waveform signal between this point and the local maxima point would be used in the non-negative least-square Gaussian fitting. However, if both of the local range points are below $y_{Lc.Max}$, we would use the side with lower $\overline{y_{left}}$ or $\overline{y_{right}}$ as the segmented signal for least-square fitting. The one fifth criterion was selected to crop the signal to a curve, which includes the inflection points (1 sigma away from centroid). The Gaussian curve of responses below one fifth approximates a straight line, which does not provide useful shape information to recover the initial descriptor of Gaussian functions.

The least-square fitting converts a non-linear Gaussian relation into a linear relation as shown in Eq. (14) below, so traditional non-negative least-square fitting could be used.

$$(2 * \delta_n^2) * \log\frac{y}{a_n} = -(x - c_n)^2 \tag{14}$$

The position $x_{Lc.Max}$ and response $y_{Lc.Max}$ of the local maxima point are used in Eqs. (4) and (5) to calculate the centroid c_n and amplitude a_n of this node and solve the equation for standard deviation δ_n. On the other hand, if the Gaussian peak is superimposed on a high response, Eqs. (6) and (8) are used.

In the linear adjustment procedure mentioned above, not all Gaussian nodes are strongly impacted by their neighbors. It is important to evaluate the severity of deformation from the response of the adjacent node, order these factors and apply adjustments based on this order.

We evaluate the deformation impact of each node pair by looking at the overlapping range of adjacent nodes. We notice that a low response is usually observed in the range between 1.75 and 3.5 standard deviations from the Gaussian center, which possesses high curvature values. This range is hence more prone to introduce deformation to their adjacent nodes. We also found that inflection point detection, which is used to initially estimate the parameters of Gaussian nodes, is significantly affected when current node is within a standard deviation away from its adjacent Gaussian center. Based on these facts, the following procedure is designed and implemented to estimate the deformation impact on each node. In Fig. 3, we are evaluating deformation impact on the right node, which is also plotted in Fig. 3c.

(a) Compute the Gaussian response of all adjacent nodes (Fig. 3a). For the adjacent node, line up the points, which are 1.75 and 3.5 standard deviation ($e.g.\{x_{1.75w\_left}, y_{1.75w\_left}\}$) away from the current Gaussian center as below (Fig. 3b):

$$\{x_{1.75w\_left}, y_{1.75w\_left}\}, \{x_{3.5w\_left}, y_{3.5w\_left}\}$$

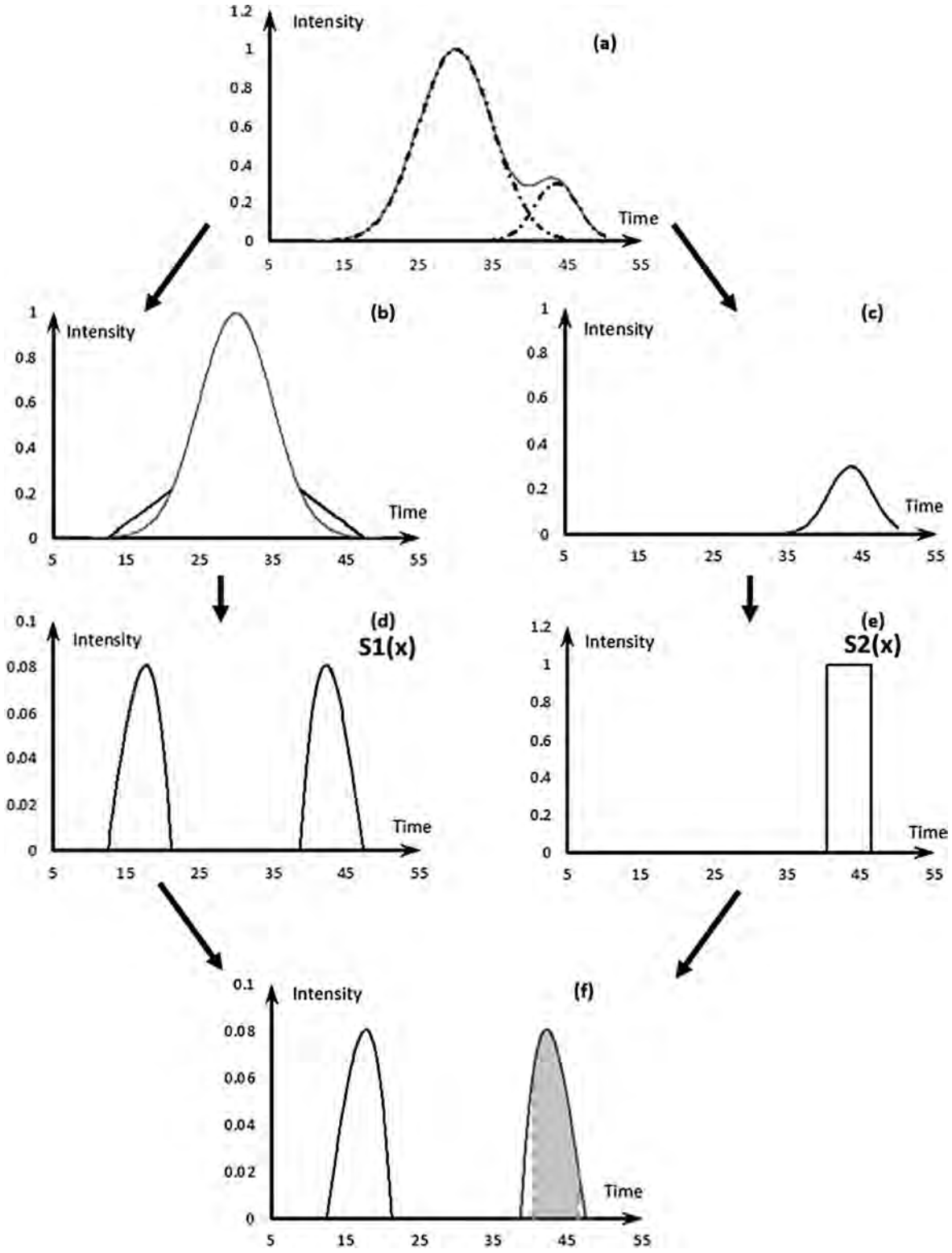

Fig. 3. Quantification of deformation from node right in (a) to node left. The ranges covered by the straight-line segments of node left are very sensitive to additive signals, which possesses high curvature. The active range of S2(x) is designed to be the high curvature range of node right. We are using the area affected by this high-curvature range to measure the deformation from the right node to the left.

$\{x_{3.5w\_right}, y_{3.5w\_right}\}$, $\{x_{1.75w\_right}, y_{1.75w\_right}\}$,

(b) Compute the difference between this line and the response curve of Gaussian node (Fig. 3d). We denote it as Function $S_1(x)$.

(c) Generate a rectangle waveform of response value 1, between position $\{x_{1w\_left}, y_{1w\_left}\}$ and $\{x_{1w\_right}, y_{1w\_right}\}$, whic a_j h are within a standard deviation away from the Gaussian centroid of the currently assessed node (Fig. 3e). We denote this waveform as Function $S_2(x)$.

(d) Find the intersection between non-zero ranges of two functions $S_1(x) and S_2(x)$, and name this range as $[x_1, x_2]$ (Fig. 3f). So we can compute the normalized deformation impact from node i (left) to node j (right) in Eq. (15). We normalize the equation with amplitude a_i and, so a node j of higher amplitude or a node i of lower amplitude will introduce more deformation impact to node i.

$$I_{ij} = \int_{x_1}^{x_2} S_1(x) * S_2(x) dx * \frac{a_i}{a_j} \tag{15}$$

(e) Compute total deformation impact on node j by summing up deformation impacts from all its adjacent nodes:

$$I_j = \sum_{i=1}^{j-1} I_{ij} + \sum_{i=j+1}^{n} I_{ij} \tag{16}$$

(f) Rank total deformation impacts of all nodes increasingly. Linearly adjust initially fitted nodes based on this order.

2.2.3. Non-linear final optimization step

The final non-linear optimization step is designed to fine-tune the fitted Gaussian nodes. It is built on the non-negative LM optimization, which has been widely used in the literature for parameter adjustment of non-linear curve fitting. Our final non-linear optimization step is carried out on the noisy original waveform. With the previously linearly adjusted Gaussian nodes, it is less probable to trap the LM iteration in a state of local minimal error. Furthermore, it is expected that lower number of iterations are needed to be carried out in the LM optimization. A last check is triggered to avoid missing nodes by looking at fit residuals. The absolute maximum value is estimated from the difference between LM optimized fitting and the original noisy raw input waveform. If the absolute maximum value is greater than three times the standard deviation of the noise signal, a node fitting procedure would be used on the smoothed residual waveform (following previously mentioned procedures). If new nodes are added, the non-negative LM optimization would be carried out once again to adjust the final Gaussian fits.

2.3. Accuracy assessment

Our LAIGD method is compared with the typical Gaussian decomposition method which in this paper would be abbreviated as the GD method. The GD method has been extensively used for analyzing LVIS signals and associated LVIS-derived products. As a sensor similar to LVIS will be shortly installed on the International Space Station through the Global Ecosystems Dynamics Investigation Lidar (GEDI) mission we wanted to contrast our methodology with the prevailing method associated with LVIS data products.

Three statistical error estimations are calculated to evaluate the waveform regression results, namely root-mean-square-error (RMSE), relative squared error (RSE) (Lehmann, 2006) and relative RMSE (rRMSE) (Klein, 1991), calculated as:

$$RMSE = \sqrt{\frac{1}{N}\sum (y - \hat{y})^2} \tag{17}$$

$$RSE = \frac{\sum (y - \hat{y})^2}{\sum (y)^2} \tag{18}$$

$$rRMSE = \sqrt{\frac{1}{N}\sum ((y - \hat{y})/y)^2} * 100\% \tag{19}$$

where $\hat{y}$ is the fitted response using LAIGD method and N the total number of samples. The accuracy statistics are calculated only using the waveform segment, the responses of which are greater than three times the standard deviation of background noise signals.

Though RMSE is a popular formula to measure the error rate of regression models, this variable, however, would only reflect the absolute error. The waveforms, in our case, have different maximum responses and overall signal strength. Thus, we also bring RSE and rRMSE in the evaluation process. RSE, used as a normalized error rate, compares the errors from different waveform with different area and variation. The rRMSE measures the relative error of different data. For the same amount of absolute error, the lower input waveform response, the higher the rRMSE would be.

3. Datasets

Two datasets were used in our study, one containing airborne LVIS data and another simulated dataset to examine further algorithmic improvements.

Airborne LVIS Data. Accuracy assessment took place on a wide variety of LiDAR waveforms from different land cover types. The data acquisition was performed in August 24–26, 2009 in the Onondaga county, NY using a LVIS laser scanner. The LVIS sensor is a full-waveform laser scanner, which records from transmitted pulse to ground returned echoes completely. Within each waveform, a total of 432 time bins were recorded. The scanner's fixed beam divergence produces an average footprint size of 20 m. The laser pulse wavelength is 1064 nm. The sampling frequency is 1 GHz leading to the vertical resolution of 0.15 m. The specifications of the airborne LVIS full-waveform laser scanner are presented in Blair et al. (1999b). The sampled areas were selected based on the visual interpretation of aerial images and discrete return LiDAR data. A total of 4166 plots (i.e. LVIS footprints) were sampled, including 1096 for deciduous forest, 554 for coniferous forest, 986 for shrub canopy, 230 for grass, 634 for residential and 666 for urban area.

Synthetic LiDAR Data. To evaluate further model performance 9600 computer-generated LiDAR full-waveforms were assessed. These samples are designed to mimic the real returned waveforms with different levels of complexity. The synthetic waveforms are generated with similar noise level and sampling rate as LVIS waveform data. This gives our synthetic waveform similar sampling deformation (i.e. sampling smooths out the signals of higher frequency than sampling rate) and Gaussian standard deviation as the LVIS waveform signals. Noise is introduced with an absolute standard deviation value 0.5 and the sampling rate is set to 0.1 ns. The synthetic LiDAR waveforms are composed of Gaussian nodes with a count between one and five. The standard deviation of each Gaussian function is between 0.17 ns and 1 ns, which is concluded from the real LVIS data and greater than the standard deviation of the transmitted pulse. The minimum distances between each Gaussian centers are equally distributed between 0 and 6 ns. The total area below the final waveform is set to be a fixed value of 160 to normalize the amplitude of each Gaussian function based on their standard deviation values and areas beneath their individual Gaussian curve.

4. Results and discussion

4.1. Decomposition accuracy of observed LVIS data

The LVIS sensor characteristics are similar to the planned NASA mission to install the Global Ecosystem Dynamics Investigation Lidar (GEDI) on the International Space Station. The scientific goal of GEDI is to "improve quantification and understanding of the

Earth's carbon cycle and biodiversity". Therefore, of particular interest is algorithmic performance over vegetated classes to assess forest vertical profile decomposition. Table 1 and Fig. 4 present a comparison of our proposed method with the prevailing Gaussian decomposition method (Hofton et al., 2000), referred to as the GD method. The RMSE, RSE and rRMSE statistics suggest that the decomposition derived from the LAIGD method exhibits considerable less error that the one derived using the GD method. The RMSE values of coniferous, deciduous and shrub types are 1.065, 1.074 and 1.309, respectively. These values are approximately two to three times of the standard deviation of the constant background noise, which is 0.47. Consequently, not only our results offer considerable improvements over the existing method but they are also approaching the limits of optimal decomposition considering the error magnitude proximity to the signal noise.

The RSE statistic allows us to compare regression accuracy among different land cover types as it is a normalized error rate. Two encouraging observations can be made. First, the coniferous error is now similar to the deciduous one. Coniferous vertical structure and density have been resulted into more challenging biomass estimations (Zhuang et al., 2015). Secondly, decomposition errors for shrubs have been greatly reduced. Shrubs, while with lower carbon stock compared to forests, offer significant biodiversity benefits as crucial wildlife habitats, especially for avian biodiversity (Hyde et al., 2005; Pinotti et al., 2012). Looking more closely at relative class performance, the deciduous forests are composed of multiple canopy layers with different optical thickness and overlap. Compared with ground surfaces or other man-made surface, the returned pulses have relatively lower amplitude, wider standard deviation. The derivative points in smoothed waveform of deciduous forest would be less affected by sampling deformation, which effectively contribute to the good fit of the GD method. On the other hand, the relatively lower response from deciduous forest would also lead to a lower absolute error, when the bias is at the same level. This could, in some extent, account for the lower error in vegetation canopies and higher errors in urban and residential types for our method.

The rRMSE statistic offers a complementary view in algorithmic performance in weak signal responses. Among all classes the proposed method clearly outperforms the benchmark. Relatively higher rRMSE values can be observed in grass, residential and urban classes. A possible reason may be that the waveforms from those types are mostly separate peaks with limited overlap, therefore there is a higher chance to include a high proportion of signal points with weak responses in these waveforms.

4.2. Decomposition accuracy of synthetic data

The synthetic data are generated with Gaussian nodes of known centroid, standard deviation and amplitude. Here, we compare the characteristics of the identified nodes from our LAIGD method and the GD method with the known node parameters. To further assess performance across waveforms of different complexity, the synthetic waveforms are grouped by number of Gaussian nodes and degree of overlap. The degree of overlap is defined as the ratio between the waveform area occupied from overlapping Gaussians and the waveform area covered by the entire waveform. The overlapping ranges are the intersection among each Gaussian node with three standard deviation buffers.

Tables 2–4 exhibit fitting accuracy improvements of the proposed method versus the benchmark. Dashes indicate cases not tested due to limited (or no) applicability (e.g. in the first row a single node cannot have overlap). Each cell in the tables expresses the average over 200 simulations. A clear pattern emerges: as signal complexity increases, demonstrated by higher number of nodes and signal overlap, so do the improvements offered by our method. In complex signals the improvements can reach 50% or higher. When there is only one Gaussian node or two Gaussian nodes without any overlap, our method may underperform.

This could be attributed to the GD fitting process, where more nodes are used than required. This overfitting behavior of the GD method might be due to its strict node identification criteria to detect the overlapping node in a single search. This may cause the GD method to detect a higher number of node candidates than the actual number to make sure there is no undetected node.

The accuracy of the top and ground returns was evaluated using the proposed and benchmark decomposition results and their contrast with the synthetic data. With respect to ground detection, the obtained results in Table 5 indicate a considerable improvement for the proposed method. The "greedy" approach followed by the GD benchmark method fails to accurately detect ground returns in overlapping nodes. In contrast, the proposed method offers consistent results that are affected to a much lesser degree by the signal complexity. In the ground case the return signal may be mixed with delayed above ground object returns (e.g. signal bouncing inside lower canopy before reaching sensor) and/or low height objects (e.g. shrubs) (Zhuang and Mountrakis, 2014a). Therefore, the observed improvements in ground return identification are a significant step forward for waveform LiDAR processing. Considering the importance that ground return identification plays in various LiDAR-derived products, such as canopy height, biomass estimation, carbon pools measurement and hydrological topography we consider ground identification improvements offered by our method as the most important advancement offered by our approach.

The top return was defined as three half widths from the center of the first Gaussian and the ground return was defined as the center of the last Gaussian. Results from the top return accuracy estimation are provided in Table 6. We should note that the top return detection task is not as challenging as the ground return detection as the top return signal is not distorted by the different object layers. Since top return is a relatively easy task our intention is not to demonstrate a significant outperformance of our proposed method, rather that it is consistent with the GD approach and does

Table 1
Error averages per land class for the proposed and benchmark methods.

		RMSE		RSE ($*10^{-3}$)		rRMSE ($*10^{-2}$)	
Land cover	Number of waveforms	LAIGD	GD	LAIGD	GD	LAIGD	GD
Coniferous	554	1.065	2.126	0.986	2.301	0.252	0.989
Deciduous	1096	1.074	1.251	0.984	1.234	0.293	0.424
Shrub	986	1.309	3.272	0.420	1.850	0.301	1.837
Grass	230	2.076	5.961	0.536	2.399	1.080	4.744
Residential	634	2.948	3.701	1.170	3.711	0.590	2.490
Urban	666	1.965	3.061	3.130	6.110	1.016	3.765
Weighted average[a]		1.528	2.768	1.198	2.742	0.494	1.921

[a] Weighted by the proportion of sample size of each land cover type.

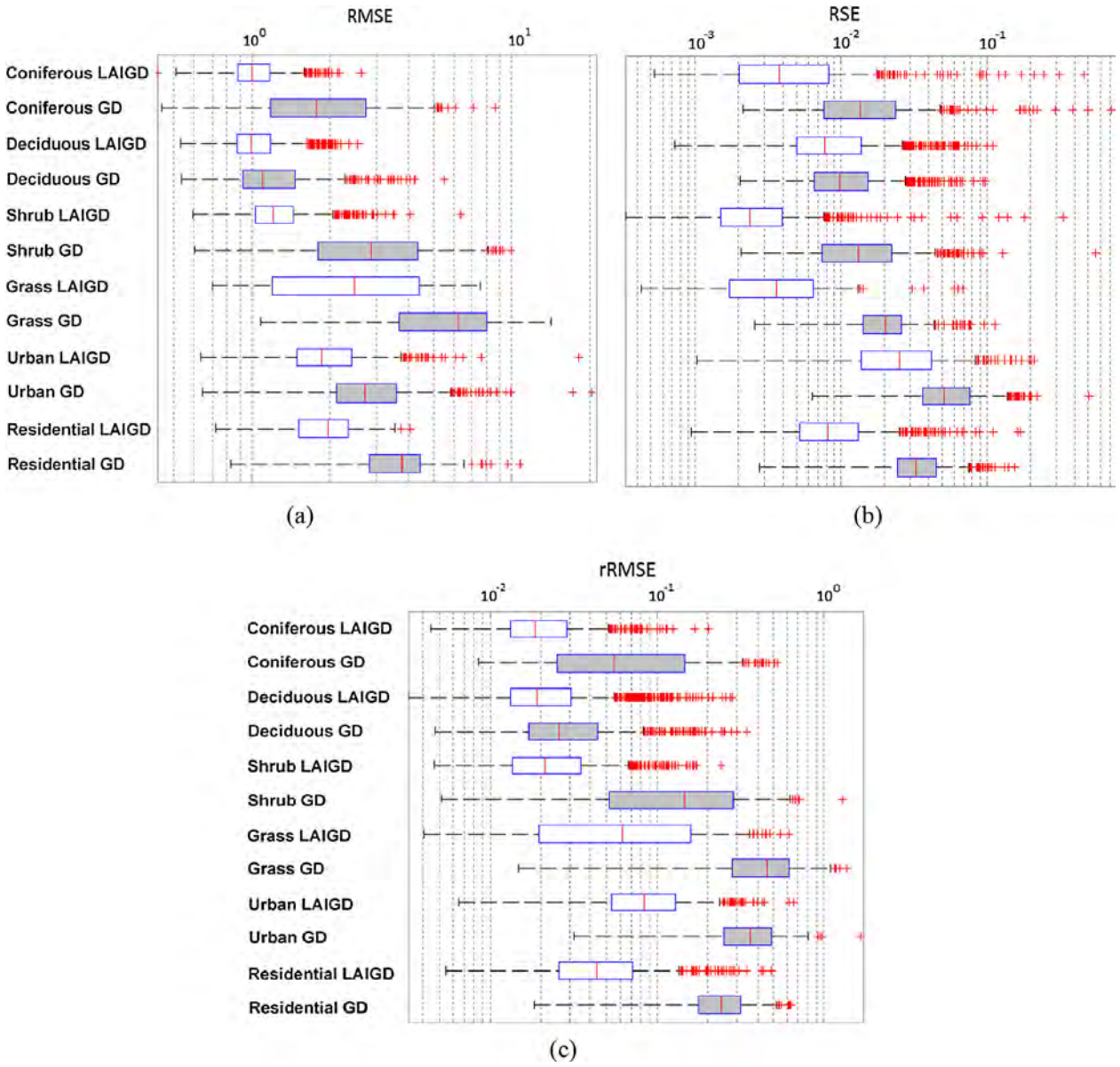

Fig. 4. Logarithmic box plots of RMSE, RSE and rRMSE on different land cover types using the GD and our LAIGD method. Rectangles depict 25, 50 and 75 percentiles, outer lines 10 and 90 percentiles, outliers visualized as red crosses. (For interpretation of the references to color in this figure legend, the reader is referred to the web version of this article.)

Table 2
RMSE percent decrease of LAIGD over the GD benchmark method.

Number of nodes	Degree of overlap										Average
	None	(0, 0.1]	(0.1, 0.2]	(0.2, 0.3]	(0.3, 0.4]	(0.4, 0.5]	(0.5, 0.6]	(0.6, 0.7]	(0.7, 0.8]	(0.8, 0.9]	
1	−3.5%	–	–	–	–	–	–	–	–	–	−3.5%
2	−7.0%	10.4%	3.0%	14.3%	13.1%	15.8%	27.9%	51.3%	58.7%	58.1%	24.6%
3	12.9%	19.2%	11.8%	14.0%	16.6%	20.1%	26.7%	34.7%	40.8%	38.8%	23.6%
4	22.0%	23.7%	17.8%	19.3%	18.9%	26.8%	27.8%	28.2%	33.7%	31.9%	25.0%
5	–	32.8%	26.1%	28.2%	24.1%	23.8%	21.2%	23.0%	25.2%	25.5%	25.5%
6	–	–	31.6%	31.0%	29.5%	29.0%	26.6%	28.2%	27.0%	22.6%	28.2%
Average	6.1%	21.5%	18.1%	21.3%	20.4%	23.1%	26.0%	33.1%	37.1%	35.4%	24.6%

not produce any unexpected errors. Performance between the two decomposition methods is comparable with a small benefit offered by the proposed approach. As signal complexity increases so does the distance error.

4.3. Execution time

A last item for consideration is execution time. We should emphasize that neither of the algorithms are optimized for execution speed therefore readers should concentrate on general relative

Table 3
RSE percent decrease of LAIGD over the GD benchmark method.

Number of nodes	Degree of Overlap										Average
	None	(0, 0.1]	(0.1, 0.2]	(0.2, 0.3]	(0.3, 0.4]	(0.4, 0.5]	(0.5, 0.6]	(0.6, 0.7]	(0.7, 0.8]	(0.8, 0.9]	
1	9.7%	–	–	–	–	–	–	–	–	–	9.7%
2	−36.4%	11.0%	6.7%	21.8%	30.8%	30.5%	46.4%	79.4%	77.0%	79.5%	34.7%
3	8.0%	32.7%	12.2%	17.0%	27.7%	27.2%	40.2%	54.7%	59.0%	61.5%	34.0%
4	34.9%	35.5%	23.6%	23.5%	24.3%	40.0%	37.2%	34.9%	43.5%	44.1%	34.1%
5	–	58.5%	41.0%	47.8%	31.3%	27.4%	29.2%	31.4%	29.7%	33.7%	36.7%
6	–	–	49.9%	46.8%	48.0%	48.8%	36.8%	36.3%	35.1%	31.7%	41.7%
Average	4.0%	34.4%	26.7%	31.4%	32.4%	34.8%	38.0%	47.3%	48.9%	50.1%	35.5%

Table 4
rRMSE percent decrease of LAIGD over the GD benchmark method.

Number of nodes	Degree of Overlap										Average
	None	(0, 0.1]	(0.1, 0.2]	(0.2, 0.3]	(0.3, 0.4]	(0.4, 0.5]	(0.5, 0.6]	(0.6, 0.7]	(0.7, 0.8]	(0.8, 0.9]	
1	−4.8%	–	–	–	–	–	–	–	–	–	−4.8%
2	37.6%	22.6%	18.4%	46.1%	32.2%	44.8%	52.9%	79.7%	80.4%	80.7%	49.5%
3	58.3%	49.0%	52.5%	56.1%	56.4%	56.1%	58.9%	70.4%	72.4%	63.6%	59.4%
4	60.6%	60.6%	48.1%	52.6%	54.7%	61.8%	58.5%	61.0%	66.6%	62.5%	58.7%
5	–	66.2%	58.1%	61.6%	54.5%	58.5%	54.9%	54.9%	55.6%	54.9%	57.7%
6	–	–	60.4%	58.6%	60.3%	60.1%	56.9%	57.8%	52.0%	52.5%	57.3%
Average	37.9%	49.6%	47.5%	55.0%	51.6%	56.3%	56.4%	64.8%	65.4%	62.8%	55.2%

Table 5
Average distance in waveform sampling units between the detected and actual location of ground return position. LAIGD method in text and GD method in parentheses.

Distance (in Sampling Unit)											
Number of nodes	Degree of overlap										Average
	None	(0, 0.1]	(0.1, 0.2]	(0.2, 0.3]	(0.3, 0.4]	(0.4, 0.5]	(0.5, 0.6]	(0.6, 0.7]	(0.7, 0.8]	(0.8, 0.9]	
1	0.1 (0.9)	–	–	–	–	–	–	–	–	–	0.0 (0.9)
2	0.1 (1.6)	0.1 (5.7)	0.2 (7.0)	0.3 (8.9)	0.3 (9.7)	1.0 (10.7)	1.2 (11.2)	1.4 (12.2)	2.4 (13.0)	3.2 (13.2)	1.0 (9.30)
3	0.6 (9.9)	0.7 (9.6)	0.7 (9.5)	0.8 (10.4)	0.9 (11.5)	1.1 (11.7)	1.5 (12.6)	1.9 (12.7)	2.5 (12.8)	2.7 (13.2)	1.3 (11.4)
4	0.7 (11.3)	0.2 (9.9)	1.1 (10.4)	0.8 (10.4)	0.8 (10.7)	0.8 (10.8)	2.1 (11.2)	2.2 (12.0)	2.1 (12.5)	2.6 (12.3)	1.3 (11.2)
5	–	1.9 (11.1)	0.9 (10.6)	1.6 (10.5)	0.9 (10.6)	1.4 (11.3)	2.2 (11.4)	1.7 (11.3)	2.4 (11.5)	2.6 (11.9)	1.7 (11.1)
6	–	–	1.3 (11.1)	0.9 (10.7)	1.0 (11.4)	1.2 (10.7)	1.2 (11.0)	1.8 (11.3)	1.9 (11.6)	2.9 (11.6)	1.5 (11.2)
Average	0.3 (5.9)	0.7 (9.1)	0.8 (9.7)	0.9 (10.2)	0.8 (10.8)	1.1 (11.0)	1.7 (11.5)	1.8 (11.9)	2.3 (12.3)	2.8 (12.5)	1.3 (10.6)

Table 6
Average distance in waveform sampling units between the detected and actual location of top return position. LAIGD method in text and GD method in parentheses.

Distance (in Sampling Units)											
Number of nodes	Degree of overlap										Average
	None	(0, 0.1]	(0.1, 0.2]	(0.2, 0.3]	(0.3, 0.4]	(0.4, 0.5]	(0.5, 0.6]	(0.6, 0.7]	(0.7, 0.8]	(0.8, 0.9]	
1	0.2 (0.2)	–	–	–	–	–	–	–	–	–	0.2 (0.2)
2	1.8 (1.8)	1.4 (4.8)	1.8 (4.1)	1.1 (3.3)	1.3 (3.2)	1.1 (2.9)	2.2 (3.9)	2.0 (4.6)	3.6 (5.9)	4.2 (7.0)	2.1 (4.2)
3	2.0 (2.0)	2.7 (2.5)	2.8 (3.5)	2.9 (3.7)	2.4 (3.7)	3.2 (3.9)	3.3 (4.1)	3.5 (4.7)	6.7 (7.9)	6.5 (11.0)	3.6 (4.7)
4	2.7 (2.6)	4.1 (4.2)	2.5 (2.4)	3.2 (3.3)	3.3 (3.3)	3.4 (3.0)	4.2 (4.3)	4.4 (4.6)	6.7 (6.9)	7.3 (7.8)	4.2 (4.2)
5	–	3.9 (3.7)	3.4 (3.3)	4.7 (4.5)	4.3 (3.8)	3.2 (3.2)	5.8 (5.7)	5.7 (5.6)	6.6 (6.8)	8.1 (8.4)	5.1 (5.0)
6	–	–	4.1 (4.1)	4.4 (4.2)	3.9 (3.7)	4.7 (4.4)	4.2 (4.0)	5.0 (5.1)	6.5 (5.9)	6.3 (6.8)	4.9 (4.8)
Average	1.7 (1.7)	3.1 (3.8)	2.9 (3.5)	3.3 (3.8)	3.0 (3.5)	3.1 (3.5)	3.9 (4.4)	4.1 (4.9)	6.0 (6.7)	6.5 (8.2)	3.8 (4.5)

execution time differences and not absolute execution times. Table 7 contrasts execution time without any multi-thread optimization involved. While none of the methods is specifically optimized for execution time suggesting that there is room for improvement, we can conclude that our method is approximately twice as fast as the GD approach. We attribute these improvements to the proposed method's ability to lower the redundancy in the detected Gaussian nodes by using the iterative linear procedure, so a lower number of parameters with good approximations are forwarded to the time-consuming non-linear LM optimization in the last step. The speed advantage of our method is especially important considering application of the proposed method to upcoming high-volume satellite-derived GEDI observations. Finally, as expected, both methods become more time-intensive as signal complexity increases.

5. Conclusion

In this paper, a linearly approximated iterative Gaussian Decomposition method (LAIGD) has been created to fit and decompose full-waveform LiDAR signals into a set of single Gaussian

Table 7
Code execution time of the LAIGD method and GD method (in parenthesis). Note none of the methods are optimized, results should be used only for relative comparisons between the two methods.

Code execution time (in seconds per waveform)											
Number of nodes	Degree of overlap										Average
	None	(0, 0.1]	(0.1, 0.2]	(0.2, 0.3]	(0.3, 0.4]	(0.4, 0.5]	(0.5, 0.6]	(0.6, 0.7]	(0.7, 0.8]	(0.8, 0.9]	
1	0.3 (0.1)	–	–	–	–	–	–	–	–	–	0.3 (0.1)
2	0.4 (0.3)	0.4 (0.7)	0.4 (0.6)	0.5 (0.4)	0.5 (0.4)	0.5 (0.4)	0.6 (0.4)	0.6 (0.3)	0.6 (0.2)	0.4 (0.1)	0.5 (0.4)
3	0.6 (1.2)	0.5 (2.4)	0.6 (2.5)	0.6 (2.4)	0.7 (1.8)	0.7 (1.8)	0.7 (1.9)	0.7 (1.0)	0.7 (0.9)	0.6 (0.6)	0.6 (1.6)
4	0.8 (2.0)	0.9 (2.9)	1.0 (4.0)	1.0 (4.0)	1.0 (3.9)	1.1 (3.9)	1.1 (3.9)	1.1 (3.0)	1.1 (2.3)	0.9 (1.7)	1.0 (3.2)
5	–	1.6 (3.1)	1.8 (4.8)	2.0 (6.0)	2.2 (6.4)	2.6 (5.8)	2.6 (5.8)	2.5 (5.9)	2.4 (5.7)	2.1 (3.1)	2.2 (5.3)
6	–	–	5.0 (5.0)	4.2 (4.9)	3.1 (4.9)	4.6 (5.0)	4.7 (5.0)	4.4 (5.9)	4.3 (6.9)	3.9 (7.0)	4.3 (5.6)
Average	0.5 (0.9)	0.9 (2.2)	1.8 (3.4)	1.7 (3.6)	1.5 (3.5)	1.9 (3.4)	1.9 (3.5)	1.9 (3.2)	1.8 (3.2)	1.6 (2.5)	1.6 (3.0)

nodes. Initially, we assumed each Gaussian node is superimposed on a complete or a piecewise first-order linear function (a straight-line segment), while fitting the parameters of Gaussian nodes with cropped waveform. The fitted parameters of Gaussian nodes are then linearly adjusted based on the overlaps with their adjacent nodes. By using this two-step iterative structure, new nodes are continuously discovered from the residual waveform between the original input waveform and the previously adjusted fitting until a good fit is achieved. By using a non-linear LM optimization, the final parameter estimates are generated. Our LAIGD method is then tested with LVIS large-footprint full-waveform data, which have been manually classified into six land cover types. Most of the waveforms are fitted with RMSE values smaller than three standard deviation of the noise signal. The RMSE, RSE and rRMSE values for the LAIGD method from all land classes are lower than those from the GD method, where RMSE improvements from each class range from 14.1% lower in the deciduous class to 65.2% lower in the grass class. The rRMSE values also shows better performance of LAIGD method in fitting the tail section of waveforms. From the tests of using 9600 synthetic noisy waveforms with different number of nodes and degrees of overlap, our LAIGD method shows higher improvement as signal complexity increases. From the comparisons with actual node parameters from the synthetic waveforms, we find that LAIGD provides better fitting characteristics and better performance in detecting the first and last nodes, which are critical features in multiple LiDAR product creation. Finally, the multi-step iterative LAIGD method reduces computation times in half compared to the GD method. To conclude, the proposed method could significantly improve waveform LiDAR signal processing, both in terms of accuracy and execution speed.

Acknowledgements

This work was supported through NASA's Biodiversity Program [grant number NNX09AK16G]. The authors thank Dr. Zhuang for providing the LVIS dataset along with associated land cover classification reference and Dr. Bevilacqua for helpful discussions on the design of the accuracy evaluation.

References

Ahmed, R., Siqueira, P., Hensley, S., 2013. A study of forest biomass estimates from lidar in the northern temperate forests of New England. Remote Sens. Environ. 130, 121–135.

Alexander, C., Tansey, K., Kaduk, J., Holland, D., Tate, N.J., 2010. Backscatter coefficient as an attribute for the classification of full-waveform airborne laser scanning data in urban areas. ISPRS J. Photogram. Remote Sens. 65 (5), 423–432.

Blair, B.J., Hofton, M.A., 1999a. Modeling laser altimeter return waveforms over complex vegetation using high-resolution elevation data. Geophys. Res. Lett. 26 (16), 2509–2512.

Blair, B.J., Rabine, D.L., Hofton, M.A., 1999b. The Laser Vegetation Imaging Sensor: a medium-altitude, digitisation-only, airborne laser altimeter for mapping vegetation and topography. ISPRS J. Photogram. Remote Sens. 54 (2), 115–122.

Castillo, M., Rivard, B., Sánchez-Azofeifa, A., Calvo-Alvarado, J., Dubayah, R., 2012. LIDAR remote sensing for secondary Tropical Dry Forest identification. Remote Sens. Environ. 121, 132–143.

Castillo-Núñez, M., Sánchez-Azofeifa, G.A., Croitoru, A., Rivard, B., Calvo-Alvarado, J., Dubayah, R.O., 2011. Delineation of secondary succession mechanisms for tropical dry forests using LiDAR. Remote Sens. Environ. 115, 2217–2231.

Chauve, A., Mallet, C., Bretar, F., Durrieu, S., Deseilligny, M.P., Puech, W., 2007. Processing full-waveform LiDAR data: modelling raw signals. Int. Arch. Photogram., Remote Sens. Spat. Inform. Sci., 102–107

Chen, Q., 2010. Assessment of terrain elevation derived from satellite laser altimetry over mountainous forest areas using airborne lidar data. ISPRS J. Photogram. Remote Sens. 65 (1), 111–122.

Dempster, A.P., Laird, N.M., Rubin, D.B., 1977. Maximum likelihood from incomplete data via the EM algorithm. J. Roy. Stat. Soc. 39 (1), 1–38.

Drake, J.B., Dubayah, R.O., Clark, D.B., Knox, R.G., Blair, J.B., Hofton, M.A., Prince, S., 2002. Estimation of tropical forest structural characteristics using large-footprint LiDAR. Remote Sens. Environ. 79 (2), 305–319.

Ducic, V., Hollaus, M., Ullrich, A., Wagner, W., Melzer, T., 2006. 3D vegetation mapping and classification using full-waveform laser scanning. In: Proc. Workshop on 3D Remote Sensing in Forestry. EARSeL/ISPRS, Vienna, Austria, pp. 211–217.

Duong, H.V., Lindenbergh, R., Pfeifer, N., Vosselman, G., 2008. Single and two epoch analysis of icesat full waveform data over forested areas. Int. J. Remote Sens. 29 (5), 1453–1473.

Fieber, K.D., Davenport, I.J., Tanase, M.A., Ferryman, J.M., Gurney, R.J., Becerra, V.M., Walker, J.P., Hacker, J.M., 2015. Validation of Canopy Height Profile methodology for small-footprint full-waveform airborne LiDAR data in a discontinuous canopy environment. ISPRS J. Photogram. Remote Sens. 104, 144–157.

Gong, P., Li, Z., Huang, H., Sun, G., Wang, L., 2011. ICEsat GLAS data for urban environment monitoring. IEEE Trans. Geosci. Remote Sens. 49 (3), 1158–1172.

Grekousis, G., Mountrakis, G., Kavouras, M., 2015. An Overview of 21 Global and 43 Regional Land-Cover Mapping Products. Int. J. Remote Sens. 36, 5309–5335.

Hancock, S., Disney, M., Muller, J.-P., Lewis, P., Foster, M., 2011. A threshold insensitive method for locating the forest canopy top with waveform lidar. Remote Sens. Environ. 115, 3286–3297.

Harding, D.J., Lefsky, M.A., Parker, G.G., Blair, J.B., 2001. Laser altimeter canopy height profiles: methods and validation for closed-canopy, broadleaf forests. Remote Sens. Environ. 76 (3), 283–297.

Harding, D., Carabajal, C., 2005. ICESat waveform measurements of within-footprint topographic relief and vegetation vertical structure. Geophys. Res. Lett. 32 (21), L21S10. http://dx.doi.org/10.1029/2005GL023471.

Hayashi, M., Saigusa, N., Oguma, H., Yamagata, Y., 2013. Forest canopy height estimation using ICESat/GLAS data and error factor analysis in Hokkaido, Japan. ISPRS J. Photogram. Remote Sens. 81, 12–18.

Höfle, B., Hollaus, M., Hagenauer, J., 2012. Urban vegetation detection using radiometrically calibrated small-footprint full-waveform airborne LiDAR data. ISPRS J. Photogram. Remote Sens. 67, 134–147.

Hofton, M.A., Minster, J.B., Blair, J.B., 2000. Decomposition of laser altimeter waveforms. Geosci. Remote Sens., IEEE Transact. 38 (4), 1989–1996.

Huang, W., Sun, G., Dubayah, R., Cook, B., Montesano, P., Ni, W., Zhang, Z., 2013. Mapping biomass change after forest disturbance: applying LiDAR footprint-derived models at key map scales. Remote Sens. Environ. 134, 319–332.

Hudak, A.T., Strand, E.K., Vierling, L.A., Byrne, J.C., Eitel, J.U.H., Martinuzzi, S., Falkowski, M.J., 2012. Quantifying aboveground forest carbon pools and fluxes from repeat LiDAR surveys. Remote Sens. Environ. 123, 25–40.

Hyde, P., Dubayah, R., Peterson, B., Blair, J.B., Hofton, M., Hunsaker, C., Knox, R., Walker, W., 2005. Mapping forest structure for wildlife habitat analysis using waveform lidar: validation of montane ecosystems. Remote Sens. Environ. 96 (3–4), 427–437. http://dx.doi.org/10.1016/j.rse. 2005.03.005.

Jóźków, G., Toth, C., Quirk, M., Grejner-Brzezinska, D., 2014. Compression strategies for LiDAR waveform cube. ISPRS J. Photogram. Remote Sens. 99, 1–13.

Jutzi, B., Stilla, U., 2003. Laser pulse analysis for reconstruction and classification of urban objects. Int. Arch. Photogram. Remote Sens. Spat. Inform. Sci. 34.3 (W8), 151–156.

Jutzi, B., Stilla, U., 2005a. Measuring and processing the waveform of laser pulses. Optical, 194–203.

Jutzi, B., Stilla, U., 2005b. Waveform processing of laser pulses for reconstruction of surfaces in urban areas. Meas. Tech., 2 2.3.1.
Jutzi, B., Stilla, U., 2006. Range determination with waveform recording laser systems using a wiener filter. ISPRS J. Photogram. Remote Sens. 61 (1), 95–107.
Khatami, R., Mountrakis, G., Stehman, S.V., 2016. A meta-analysis of remote sensing research on supervised pixel-based land-cover image classification processes: general guidelines for practitioners and future research. Remote Sens. Environ. 177, 89–100.
Klein, John P., 1991. Small sample moments of some estimators of the variance of the Kaplan-Meier and Nelson-Aalen estimators. Scand. J. Stat., 333–340
Lefsky, M.A., Harding, D., Cohen, W.B., Parker, G., Shugart, H.H., 1999. Surface LiDAR remote sensing of basal area and biomass in deciduous forests of eastern Maryland, USA. Remote Sens. Environ. 67 (1), 83–98.
Lehmann, Erich Leo, 2006. George Casella. Theory of Point Estimation. Springer Science & Business Media.
Lim, K., Treitz, P., Wulder, M., St-Onge, B., Flood, M., 2003. LiDAR remote sensing of forest structure. Prog. Phys. Geogr. 27 (1), 88–106.
Liu, T., Im, J., Quackenbush, L.J., 2015. A novel transferable individual tree crown delineation model based on Fishing Net Dragging and boundary classification. ISPRS J. Photogram. Remote Sens. 110, 34–47.
Mallet, C., Bretar, F., 2009. Full-waveform topographic LiDAR: state-of-the-art. ISPRS J. Photogram. Remote Sens. 64 (1), 1–16.
Mallet, C., Bretar, F., Roux, M., Soergel, U., Heipke, C., 2011. Relevance assessment of full-waveform lidar data for urban area classification. ISPRS J. Photogram. Remote Sens. 66 (6), 71–84.
Matikainen, L., Lehtomäki, M., Ahokas, E., Hyyppä, J., Karjalainen, M., Jaakkola, A., Kukko, A., Heinonen, T., 2016. Remote sensing methods for power line corridor surveys. ISPRS J. Photogram. Remote Sens. 119, 10–31.
Montesano, P.M., Cook, B.D., Sun, G., Simard, M., Nelson, R.F., Ranson, K.J., Zhang, Z., Luthcke, S., 2013. Achieving accuracy requirements for forest biomass mapping: a spaceborne data fusion method for estimating forest biomass and LiDAR sampling error. Remote Sens. Environ. 130, 153–170.
Montesano, P.M., Nelson, R.F., Dubayah, R.O., Sun, G., Cook, B.D., Ranson, K.J.R., Næsset, E., Kharuk, V., 2014. The uncertainty of biomass estimates from LiDAR and SAR across a boreal forest structure gradient. Remote Sens. Environ. 154, 398–407.
Persson, A., Holmgren, J., Söderman, U., 2002. Detecting and measuring individual trees using an airborne laser scanner. Photogram. Eng. Remote Sens. 68 (9), 925–932.
Persson, Å., Söderman, U., Töpel, J., Ahlberg, S., 2005. Visualization and analysis of full-waveform airborne laser scanner data. Int. Arch. Photogram., Remote Sens. Spat. Inform. Sci. 36.3 (W19), 103–108.
Pinotti, B.T., Pagotto, C.P., Pardini, R., 2012. Habitat structure and food resources for wildlife across successional stages in a tropical forest. For. Ecol. Manage. 283, 119–127. http://dx.doi.org/10.1016/j.foreco.2012.07.020.
Ranson, K.J., Sun, G., Kovacs, K., Kharuk, V.I., 2004. Landcover attributes from ICESat GLAS data in central Siberia. Geoscience and Remote Sensing Symposium IGARSS'04. Proceedings. IEEE International., vol. 2, pp. 753–756.
Reitberger, J., Krzystek, P., Stilla, U., 2008a. Analysis of full waveform LiDAR data for the classification of deciduous and coniferous trees. Int. J. Remote Sens. 29 (5), 1407–1431.
Reitberger, J., Schnörr, C., Krzystek, P., Stilla, U., 2008b. 3D segmentation of full waveform LiDAR data for single tree detection using normalized cut. Int. Arch. Photogram., Remote Sens. Spat. Inform. Sci. 37, 77–83.
Roncat, A., Bergauer, G., Pfeifer, N., 2011. B-spline deconvolution for differential target cross-section determination in full-waveform laser scanning data. ISPRS J. Photogram. Remote Sens. 66 (4), 418–428.
Schenk, T., Csatho, B., van der Veen, C., McCormick, D., 2014. Fusion of multi-sensor surface elevation data for improved characterization of rapidly changing outlet glaciers in Greenland. Remote Sens. Environ. 149, 239–251.
Słota, M., 2015. Full-waveform data for building roof step edge localization. ISPRS J. Photogram. Remote Sens. 106, 129–144.
Strîmbu, V.F., Strîmbu, B.M., 2015. A graph-based segmentation algorithm for tree crown extraction using airborne LiDAR data. ISPRS J. Photogram. Remote Sens. 104, 30–43.
Sullivan, F.B., Palace, M., Ducey, M., 2014. Multivariate statistical analysis of asynchronous lidar data and vegetation models in a neotropical forest. Remote Sens. Environ. 154, 368–377.
Sun, G., Ranson, K.J., 2000. Modeling lidar returns from forest canopies". IEEE Trans. Geosci. Remote Sens. 38 (6), 2617–2626.
Sun, G., Ranson, K.J., Guo, Z., Zhang, Z., Montesano, P., Kimes, D., 2011. Forest biomass mapping from lidar and radar synergies. Remote Sens. Environ. 115, 2906–2916.
Suomalainen, J., Hakala, T., Kaartinen, H., Räikkönen, E., Kaasalainen, S., 2011. Demonstration of a virtual active hyperspectral LiDAR in automated point cloud classification. ISPRS J. Photogram. Remote Sens. 66 (5), 637–641.
Swatantran, A., Dubayah, R., Roberts, D., Hofton, M., Blair, J.B., 2011. Mapping biomass and stress in the Sierra Nevada using lidar and hyperspectral data fusion. Remote Sens. Environ. 115, 2917–2930.
Tang, H., Brolly, M., Zhao, F., Strahler, A.H., Schaaf, C.L., Ganguly, S., Zhang, G., Dubayah, R., 2014. Deriving and validating Leaf Area Index (LAI) at multiple spatial scales through lidar remote sensing: a case study in Sierra National Forest, CA. Remote Sens. Environ. 143, 131–141.
Tang, H., Dubayah, R., Swatantran, A., Hofton, M., Sheldon, S., Clark, D.B., Blair, B., 2012. Retrieval of vertical LAI profiles over tropical rain forests using waveform lidar at La Selva, Costa Rica. Remote Sens. Environ. 124, 242–250.
Tang, H., Ganguly, S., Zhang, G., Hofton, M.A., Nelson, R.F., Dubayah, R., 2016. Characterizing leaf area index (LAI) and vertical foliage profile (VFP) over the United States. Biogeosciences 13, 239–252.
Wagner, W., 2010. Radiometric calibration of small-footprint full-waveform airborne laser scanner measurements: Basic physical concepts. ISPRS J. Photogram. Remote Sens. 65 (6), 505–513.
Wagner, W., Ullrich, A., Ducic, V., Melzer, T., Studnicka, N., 2006. Gaussian decomposition and calibration of a novel small-footprint full-waveform digitising airborne laser scanner. ISPRS J. Photogram. Remote Sens. 60 (2), 100–112.
Wang, C., Li, Q., Liu, Y., Wu, G., Liu, P., Ding, X., 2015. A comparison of waveform processing algorithms for single-wavelength LiDAR bathymetry. ISPRS J. Photogram. Remote Sens. 101, 22–35.
Wang, C., Tang, F., Li, L., Li, G., Cheng, F., Xi, X., 2013. Wavelet analysis for ICESat/GLAS waveform decomposition and its application in average tree height estimation. IEEE Geosci. Remote Sci. Lett. 10 (1), 115–119.
Wang, H., Glennie, C., 2015. Fusion of waveform LiDAR data and hyperspectral imagery for land cover classification. ISPRS J. Photogram. Remote Sens. 108, 1–11.
Wang, X., Huang, H., Gong, P., Liu, C., Li, C., Li, W., 2014. Forest canopy height extraction in rugged areas with ICESat/GLAS data. Geosci. Remote Sens., IEEE Transact. 52, 4650–4657.
Wang, Y., Zhang, J., Roncat, A., Künzer, C., Wagner, W., 2009. Regularizing method for the determination of the backscatter cross section in lidar data. J. Opt. Soc. Am. A 26 (5), 1071–1079.
Wulder, M.A., White, J.C., Nelson, R.F., Næsset, E., Ørka, H.O., Coops, N.C., Hilker, T., Bater, C.W., Gobakken, T., 2012. Lidar sampling for large-area forest characterization: a review. Remote Sens. Environ. 121, 196–209.
Yi, D., Harbeck, J.P., Manizade, S.S., Kurtz, N.T., Studinger, M., Hofton, M., 2015. Arctic Sea Ice freeboard retrieval with waveform Characteristics for NASA's Airborne Topographic Mapper (ATM) and Land, Vegetation, and Ice Sensor (LVIS). Geosci. Remote Sens., IEEE Transact. 53, 1403–1410.
Yu, X., Hyyppä, J., Kaartinen, H., Maltamo, M., 2004. Automatic detection of harvested trees and determination of forest growth using airborne laser scanning. Remote Sens. Environ. 90 (4), 451–462.
Zhuang, W., Mountrakis, G., 2014a. An accurate and computationally efficient algorithm for ground peak identification in large footprint waveform LiDAR data. ISPRS J. Photogram. Remote Sens. 95, 81–92.
Zhuang, W., Mountrakis, G., 2014b. Ground peak identification in dense shrub areas using large footprint waveform LiDAR and Landsat images. Int. J. Digital Earth, 1–20.
Zhuang, W., Mountrakis, G., Wiley, J., Beier, C., 2015. Estimation of aboveground forest biomass using metrics based on gaussian decomposition of waveform lidar data. Int. J. Remote Sens. 36 (7), 1871–1889.